Solar-Driven Co-Production of Hydrogen and Value-Add Conductive Polyaniline Polymer

Hongjun Chen,* Jianghui Zheng, Alfonso Ballestas-Barrientos, Jueming Bing, Chwenhaw Liao, Alexander K. L. Yuen, Chiara A. M. Fois, Peter Valtchev, Nicholas Proschogo, Stephen P. Bremner, Harry A. Atwater, Cyrille Boyer, Thomas Maschmeyer, and Anita W. Y. Ho-Baillie*

To reduce the reliance on fossil fuel, H_2, as a clean fuel, has attracted substantial research and development activities in recent years. The traditional water splitting approach requires an applied bias of more than 1.5 V and the use of ion-selective membranes to prevent the formation of a potentially explosive H_2–O_2 gas mixture, resulting in increased cost and system design complexity. Here, a solar-driven H_2 production process requiring a much lower applied bias of 1.05 V is reported whereby aniline (ANI) is oxidized to polyaniline (PANI) at the anode with a yield of 96% and H_2 evolution reaction occurs at the cathode with a faradaic efficiency of 98.6 ± 3.9%. The process has multiple advantages including the elimination of ion-exchange membrane as PANI is a solid product that also is of substantially higher value than O_2. For demonstration, a single junction perovskite solar cell and low-cost earth abundant CoP catalyst are successfully applied for this process. This process contributes to the advancement of solar-driven low-cost H_2 generation coupled with co-production of a high-value product expediting the transition to a hydrogen economy.

1. Introduction

Hydrogen (H_2) is an extremely important industrial chemical primarily used in ammonia synthesis; hydrocarbon upgrading in the petrochemical industry; the production of hydrochloric acid, reducing agent for metallic ores, shielding gas in welding, rotor coolant, lifting gas, and forming gas. H_2 is also a clean fuel, or employed as an energy carrier, whether in the form of liquid hydrogen or liquid ammonia, replacing carbon-containing fuels, thereby reducing CO_2 emissions. The concept of using H_2 as an energy carrier has generated immense research and development activities as well as investment opportunities resulting in a resurgence of efforts to create a working hydrogen economy. Clearly, carbon-free production of H_2, i.e., without the use of carbon-containing feedstock or the release of carbon-containing gas, is most desirable. Solar water splitting has been one of the conventional routes for hydrogen production.[1,2] However, in order to inhibit the formation of potentially explosive H_2–O_2 mixture gases, a diaphragm or membrane is used in an electrolyzer for the collection of O_2 or H_2 gases in separate chambers [3,4] incurring complexity, cost, and charge transfer resistance in the reaction. The oxygen evolution reaction (OER) is also a sluggish reaction and practically requires a bias ≥1.6 V in practice to drive the reaction. For a photovoltaic-driven process, 1.6 V is significantly higher than the ideal bandgap of a single junction solar cell at 1.145 or

H. Chen, J. Zheng, J. Bing, C. Liao, A. W. Y. Ho-Baillie
School of Physics
Faculty of Science
The University of Sydney
Sydney, NSW 2006, Australia
E-mail: hongjun.chen@sydney.edu.au; anita.ho-baillie@sydney.edu.au
H. Chen, J. Zheng, J. Bing, C. Liao, A. W. Y. Ho-Baillie
The University of Sydney Nano Institute
The University of Sydney
Sydney, NSW 2006, Australia

ⓘ The ORCID identification number(s) for the author(s) of this article can be found under https://doi.org/10.1002/adfm.202204807.

J. Zheng, S. P. Bremner
School of Photovoltaic and Renewable Energy Engineering
University of New South Wales
Sydney, NSW 2052, Australia
A. Ballestas-Barrientos, A. K. L. Yuen, N. Proschogo, T. Maschmeyer
School of Chemistry
The University of Sydney
Sydney, NSW 2006, Australia
C. A. M. Fois, P. Valtchev
School of Chemical & Biomolecular Engineering
The University of Sydney
Sydney, NSW 2006, Australia
C. Boyer
School of Chemical Engineering
University of New South Wales
Sydney, NSW 2052, Australia
H. A. Atwater
Department of Applied Physics and Materials Science
California Institute of Technology
Pasadena, CA 91125, USA

ADVANCED
SCIENCE NEWS
www.advancedsciencenews.com

ADVANCED
FUNCTIONAL
MATERIALS
www.afm-journal.de

1.336 eV to take the full advantage of peak energy conversion efficiencies.[5] In addition, the production of O_2 gas in water splitting has a low economic value due to its abundance in air and established routes at scale. Therefore, it is desirable to develop new strategies to reduce the intrinsic cost of H_2 production and to increase the value of the process through the production of chemicals more valuable than O_2 gas.

For this purpose, several schemes (Table S1, Supporting Information) have been reported using oxide semiconductor photoanodes to produce high-value chemicals[6–9] during H_2 production at the cathode. The products include hydrogen peroxide (H_2O_2),[10–12] peroxydisulfate ($S_2O_8^{2-}$),[13–16] hypochlorite (ClO^-),[14,17–20] Ce^{4+},[14,16] Cr^{6+},[21] Mn^{7+},[22] and 2,5-furandicarboxylic acid (FDCA).[6,23] Out of these listed work, WO_3 was regularly used as a photo-anode in the polycrystalline[14] form or as a sponge.[15,16,21,22] – the latter to increase photocurrent density and therefore reaction rate. Other types of photoanodes include $BiVO_4$[8,19,23–25] and $WO_3/BiVO_4$[10–12,17,18,20] heterojunction structure that can be modified to improve the product selectivity and conversion efficiency.[11,17,25,26] In the work by Cha et al.,[23] a mediator (2,2,6,6-tetramethylpiperidine-1-oxyl (TEMPO) for the production 2,5-furandicarboxylic acid (FDCA)) was used to reduce the voltage bias required for initiating oxidation (5-hydroxymethylfurfural (HMF)) at the photoanode ($BiVO_4$). While H_2 gas was also produced at the same time for all of these processes, in some cases, positive potentials higher than 1.23 V used in conventional water splitting for the OER are required.[6,21] In many of these processes [10–18,20–23], separators need to be used to avoid the diffusion of the products from the anodic and cathodic compartments to inhibit anodic products from being reduced at the cathode. Last, when anodic products are generated and dissolved in the electrolytes, collection and purification of these products are challenging representing barriers to low-cost and large-scale production.

In this work, we report a solar-driven co-production of H_2 gas and value-add polyaniline (PANI) polymer. PANI is one of the most common conductive polymers and has been widely used in batteries, supercapacitors, gas sensors, solar cells, and transistors.[27–30] The market value of PANI ($120–$14160 per kg) is much higher than that of O_2 gas of ($14–$16 per kg) (see Table S2, Supporting Information, for details including price of monomer).[27–31] PANI is a solid that can be easily separated from the electrolyte distinguishing our process from the above-mentioned processes for products that are dissolved in aqueous electrolyte.[6–9,21,23] This means a simple and one-chamber device can be used eliminating the use of expensive ion-selective membrane. In addition, protons are released during the aniline (ANI) polymerization reaction compensating for hydrogen evolution reaction (HER) usage[27] and therefore removing the need for acid replenishment during the reaction. While the production of PANI via electrochemical process [30–32] with the co-production of H_2 has been reported before.[33] We have demonstrated here the advantage of utilizing solar power and in particular one single-junction solar cell for such process taking advantage of lower practical bias of 1.05 V to initiate ANI polymerization, much lower than the theoretical limit (>1.23 V) for traditional water splitting. This allows single junction solar cell with close to ideal bandgap (1.145 or 1.336 eV) and/or output voltage ≈1 V to be used to take the full advantage of peak energy conversion efficiencies[5] (Figure S1, Supporting Information). In addition, the applied bias required reduces as the polymerization proceeds. This makes the process self-regulating when driven by solar as the lowering of the voltage shifts the operating point of the solar cell current–voltage curve producing higher current output, thereby, increasing higher rate of polymerization and H_2 production. Other highlights of the demonstrations in this work include the use of single junction perovskite solar cell and the use of low-cost earth-abundant CoP catalyst for the HER at the cathode. The yield of ANI polymerization on the anode was 96%. The power utilization of our demonstration was over 93%. A demonstrated faradaic efficiency of 98.6 ± 3.9% for the HER shows minimum competing side reactions even under such low operational bias. Last, a perovskite cell was encapsulated and immersed in the electrolyte as a monolithic photoanode for the purpose of demonstrating the feasibility of photovoltaic–electrochemical (PV–EC) operation with respectable stability. It is hoped that this work will inspire further developments exploring other types of conductive polymers or other value-add products that can be co-produced in a low-cost solar to hydrogen process.

2. Results and Discussion

Figure 1a illustrates the membrane-free setup for the demonstration of solar-driven co-production of H_2 gas and value-add
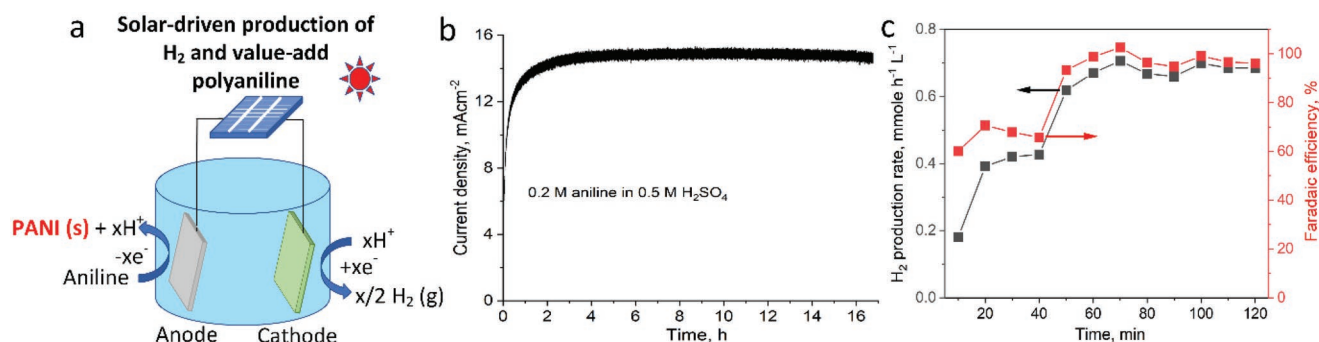
Figure 1. Solar-driven production of H_2 gas and value-add polyaniline (PANI) polymer. a) Schematic illustration of the set up that is membrane-free. For proof of concept, solar cell is placed outside the reactor to drive ANI polymerization on the anode and H_2 evolution on the cathode. b) Amperometric curves for ANI polymerization to form PANI. c) Evolved H_2 gas rate and its corresponding Faradaic efficiency.
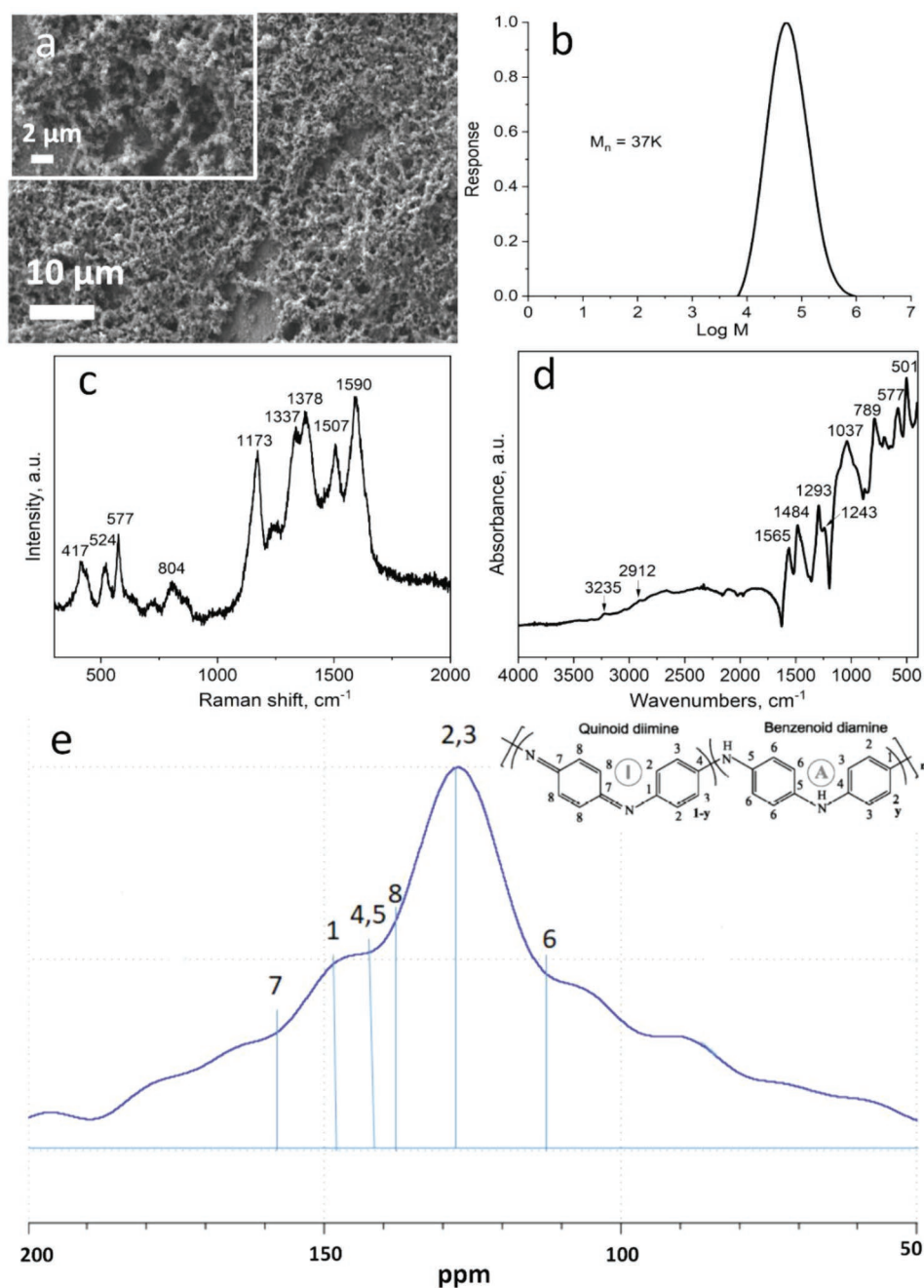
PANI polymer for proof-of-concept. The anode (a fluorine doped tin oxide (FTO) substrate or a titanium (Ti) sheet) and the cathode (a platinum sheet) are connected to the positive and negative terminal respectively of a photovoltaic device that consists of two-halves of a Si solar cell connected in series (see Figure S2, Supporting Information, for the corresponding current–density versus voltage (J–V) and power-density versus voltage (P–V) curves) outside of the reactor. The electrodes are immersed in a homogenous, aqueous solution of ANI dispersed H_2SO_4 solution. When the PV device is illuminated, the photovoltage generated drives the ANI polymerization at the anode (Figure 1b) and the HER at the cathode (Figure 1c). Figure S3a (Supporting Information) shows a photo of PANI produced on FTO confirming successful synthesis from our process. During the reaction, the FTO electrode underwent colour change from transparent to green and finally dark (Figure S3b,c, Supporting Information). Photo showing bubbles produced at the Pt electrodes is also shown in Figure S3c (Supporting Information).

The surface morphologies of the PANI were investigated by scanning electron microscopy (SEM) as shown in **Figure 2**a and Figure S4 (Supporting Information). Results reveal a relatively porous structure with agglomerates on the scale of micrometres. The molecular weight distribution of PANI was measured by the size exclusion chromatography (SEC) (Figure 2b) showing a Gaussian distribution with a number average molecular weight (Mn) centred ≈37 K. In terms of chemical compositions, Figure 2c shows a typical Raman spectrum of as-produced PANI with characteristic peaks at 577, 804, 1173, 1337, 1507, and 1590 cm^{-1} corresponding to amine deformation vibrations, benzene-ring deformations, C−H in-plane bending vibrations, C−N$^+$ vibrations of delocalized polaronic structure, N−H deformation vibrations, and C=C stretching vibrations in quinonoid ring,[27] respectively. These signals are in agreement with results obtained using Fourier-transform infrared spectroscopy as shown in Figure 2d. The bands at 789, 1037, 1293, 1484, 1565 cm^{-1} correspond to C−H deformation vibrations, −NH$^+$= , C−N$^+$ stretching vibrations, π-electrons delocalization, and quinonoid and benzenoid ring-stretching vibrations,[27] respectively. For comparison with commercially available PANI, Raman and Fourier-transform infrared (FTIR) spectra were also conducted on a commercial sample and on neutralized (by dilute ammonia solution, see details in the Experimental Section) PANI. Results are shown in Figure S5 (Supporting Information) showing good agreement suggesting respectable purity of PANI obtained in our work. Finally, solid-state nuclear magnetic resonance (NMR) spectroscopy of PANI shows its characteristic signals, which are constituted by six broad resonance signals observed at 114 (shoulder), 128, 137, 142, 147, and 157 ppm (Figure 2e)[34]. The signal at 128 ppm and shoulder at 114 ppm are assigned to carbons C-2, C-3, and C-6, respectively, which are characteristics of benzenoid diamine form (see Figure 2e). The signal at 137 ppm originates from the protonated C-8 carbon that corresponds to the quinoid part of the PANI structure as well as the signal at 157 ppm that is attributed to the non-protonated C-7 carbon.[35] The signals at 142 and 147 ppm are associated with the C-4 and C-1 non-protonated carbons, respectively.[36] In addition to these characteristic signals, we observed the presence of broad shoulder that can be attributed to the oxidation of PANI. These results confirm

that ANI monomer was successfully polymerized into PANI polymer.

To optimize the ANI polymerization process, a clean FTO substrate was used as the working electrode and a platinum sheet as the counter electrode. Cyclic voltammograms were performed and results are shown in Figure S6a (Supporting Information). In the first cycle, as the applied bias was increased from 0 to 1.6 V, current rapidly increased at 1.04 V and reached its peak at 1.36 V. This indicates that for initiating the ANI polymerization, a bias of 1.04 V is required, consistent with values (≈1.05 V) reported in the literature,[30,32,37] well below the theoretical limit of 1.23 V for water splitting. In the subsequent cycles, the initiation potential for the polymerization process was left-shifted. In addition, the curves were accompanied by three anodic peaks of PANI.[32] This suggests that the polymerization process became progressively easier (i.e., left shift implies lower potentials required) in the subsequent cycles after the formation of cation radicals in the first cycle[32,38–40] and after the growth of PANI on FTO. Further investigation into the process dynamics was conducted and will be presented below. As a control, the same test was performed without the addition of ANI in the H_2SO_4 electrolyte with the current measured being negligible (black curve in Figure S6a, Supporting Information). Therefore, the current measured during ANI polymerization is an indication of the reaction depositing PANI on the FTO electrode. The increased magnitudes of the anodic peaks also indicate that more PANI was plated on the FTO in the subsequent cycles. Figure S6b (Supporting Information) shows the amperometric curves for the ANI polymerization under different applied potentials. Again, negligible current was measured in the absence of ANI, even at 1.3 V. With ANI included, when the applied potential was >1.0 V, the current increased with applied potential until up to 1.3 V. Current also increased with time at fixed potential of more than 1.0 V and the rate is most rapid at 1.1 and 1.2 V (but slows at 1.3 V) due to the diffusion transfer limitation. This suggests that the rate of ANI polymerization process correlates with current determined by applied potential until ≈1.3 V and there is no incentive in increasing the applied potential beyond that. Apart from FTO, Ti sheet can also be used as anodic electrode taking advantage of its excellent acid-stability for longer-term operation. The onset potential for ANI polymerization remains 1.04 V (Figure S7, Supporting Information). For the purpose of illustration, a control experiment using a single Si solar cell (see Figure S8a, Supporting Information, for corresponding J–V and P–V curves) was attempted to drive ANI polymerization. As expected, the reaction did not proceed due to the low voltage from the solar cell, insufficient to initiate ANI polymerization (Figure S8b, Supporting Information).

With regards to the influence of H_2SO_4 and ANI concentrations on the polymerization process, results are shown in Figure S9 (Supporting Information). The process performed most efficiently when the concentration of H_2SO_4 ≥0.5 M suggesting the importance of proton concentration for the polymerization reaction (Figure S9a, Supporting Information). As there is no significant improvement when the concentration of H_2SO_4 was at 1 or 1.5 M, 0.5 M was the chosen concentration for the rest of the experimental work. When the ANI concentration increased from 0.1 to 0.2 M, no difference could be observed

**ADVANCED
SCIENCE NEWS**

www.advancedsciencenews.com

**ADVANCED
FUNCTIONAL
MATERIALS**

www.afm-journal.de

Figure 2. Characterization of polyaniline (PANI) polymer. a) Scanning electron microscopy (SEM) image of a representative PANI film and an enlarged view in the inset. b) PANI polymer weight distribution. c) Raman and d) Fourier-transform infrared (FTIR) spectra of PANI. e) Solid state nuclear magnetic resonance (NMR) spectrum of PANI.

in the amperometric curves in the first 5.5 h (Figure S9b, Supporting Information), reflecting similar diffusion-controlled plating behaviors. However, the current of the lower (0.1 M) ANI concentration system gradually declined while the current of the higher (0.2 M) concentration system remained constant for ≈12 h, indicating the need for a critical minimum of ANI concentration to sustain long-term polymerization. Results also show that there is no advantage of further increasing the ANI concentration to 0.4 M.

Another advantage of the process is the release of protons compensating their consumption by the HER eliminating the need for acid replenishment. To confirm this, gasses evolved from i) N_2 control, ii) H_2 control, (iii) ANI polymerization in $D_2O + D_2SO_4$, and iv) ANI polymerization in $H_2O + H_2SO_4$ were analyzed using gas chromatography-mass spectrometry (GC-MS) (details can be found in the Experimental Section). Results (Figure S10, Supporting Information) show that the aqueous electrolyte ($H_2O+H_2SO_4$) is the main contributor while

the ANI polymerization is the minor contributor to the release of protons. This explains observed electrolyte pH drop from 0.56 to 0.52 after one full day of reaction.

In addition, the process is autocatalytic[38–40] evidenced by the reduction of the bias required by the ANI polymerization as the process proceeds (Figure S6, Supporting Information) or when the electrode is already plated with PANI. To further illustrate this, pristine Ti electrode, PANI-plated Ti electrode, and PANI-plated-then-cleaned Ti electrode were compared in freshly mixed versus used electrolytes. Results are shown in Figure S11 (Supporting Information). It is clear that the polymerization process was spontaneous when using PANI-plated Ti electrode even in freshly mixed electrolyte (Figure S11b, Supporting Information). When pristine Ti electrode or PANI-plated-then-cleaned Ti electrode was used, it took 1–2 h for the polymerization process to reach its full potential (Figure S11a, Supporting Information) even in used electrolyte. Reason for improved performance using PANI-plated electrode was increased in electrochemical active surface area (ECSA) (see Figures S12b,d, Supporting Information, and caption for ECSA calculation). It was found that ECSA of the electrode was increased from 4.26 (pristine Ti) to 947.43 cm^2 (PANI-plated-Ti), which is more than 220 times after PANI plating. In addition, the presence of PANI on the electrode reduces the voltage bias required for the process to as low as 0.8 V (Figure S11c, Supporting Information). As the solar-driven polymerization proceeds, the bias required dropped from the initial 1.04 V to 0.93 V (brown square in Figure S13b, Supporting Information), then further down to 0.88 V (green circle in Figure S13b, Supporting Information) after a rudimentary electrode clean that involves partial removal of the plated-PANI followed by re-immersion of the "partially-cleaned" electrode. The drop in required voltage is consistent with what is observed in the literature.[38–40] This makes our process very different from traditional water splitting that typically requires the applied bias to be increased over time, due to the gradual degradation of catalysts driving up the over-potential required.[4,44–48]

The implication is better power utilization of the solar power. The drop in required voltage shifted the current load and therefore the operating point on the solar cell J–V curve (Figure S13b, Supporting Information) from 14.6 mA cm^{-2} (brown square) for the initial ANI polymerization and 16.2 mA cm^{-2} (green

circle) after a "rudimentary electrode clean". The power utilization ratio was then calculated using the maximum power producible by the PV device as the denominator. Power utilization increased from 93.2% to 98.7% after a rudimentary clean and reusing of the partially PANI-plated Ti electrode.

The polymerization yield was calculated based on the mass ratio of the collected and dried PANI polymer, to that of the input ANI monomer initially employed. See the Experimental Section for details regarding the precipitation of PANI. The yield was calculated to be 95.9%. It is important to note that as the plated PANI on the anode reaches a critical thickness, polymerization still proceeds and PANI will precipitate into the electrolyte in solid form.

Production of H$_2$ at the cathode during ANI polymerization was confirmed by means of gas chromatography (GC) and the Faradaic efficiency of the cell was calculated. As shown in Figure 1c, the H$_2$ evolution rate increased within the first hour with a jump at 40 min and reached saturation after 1 h. During that time, the Faradaic efficiency was calculated to be 98.6 ± 3.9%. During the 2 h measurement, no O$_2$ was detected by the GC confirming that OER did not occur as expected due to the bias being <1.23 V. This eliminates the hazard associated with the formation of an explosive H$_2$-O$_2$ gas mixture and eliminates the need for an expensive ion-selective membrane to separate the products.

To demonstrate the feasibility of PV–EC operation using a single junction solar cell for this process, an encapsulated perovskite solar cell as a monolithic photoanode immersed in the electrolyte was used to drive the reaction (**Figure 3**a). Here, the perovskite solar cell-based photoanode performs two functions: i) as a photovoltaic cell that absorbs sunlight and generates photovoltage to drive the reaction and ii) as an anode for ANI polymerization. The J–V curve of the perovskite solar cell-based photoanode is displayed in Figure S14 (Supporting Information). A two-electrode configuration was used to characterize the performance for ANI polymerization. As shown in Figure 3b, when Potential versus Pt equals to 0 V, current rapidly increases in the second and subsequent scans (red, blue, green, and purple curves) indicating nucleation growth of PANI driven by the illuminated solar cell with no external bias. The magnitude increases and the voltage required reduces in each subsequent scans as the ANI autocatalytic polymerization
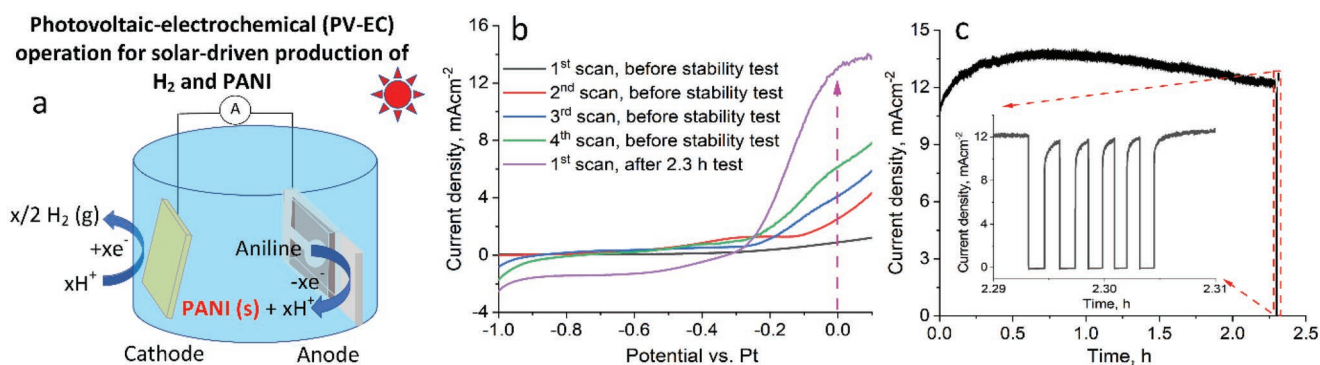
Figure 3. Photovoltaic–electrochemical (PV–EC) operation for co-production of H$_2$ gas and PANI. a) Schematic illustration of set up using a monolithic perovskite-based photoanode inside the reactor. b) Linear sweep voltammograms of the photoanode. c) Stability test for the photoanode under simulated 1-Sun irradiation for 2.3 h. The inset shows an amperometirc curve generated by a chopped light.

**ADVANCED
SCIENCE NEWS**
www.advancedsciencenews.com

**ADVANCED
FUNCTIONAL
MATERIALS**
www.afm-journal.de

process proceeds.[38–40] This observation is consistent with those from Figure S6 (Supporting Information). Figure 3c shows the amperometric curve for ANI polymerization process driven by the perovskite solar cell-based photoanode without external bias under continuous illumination. The inset shows the current density response under a "chopped light" regime, further confirming that the ANI polymerization process is entirely driven by the perovskite solar cell-based photoanode. During the measurement, the H_2 bubbles are visible and released from the Pt sheet electrode while the photoanode interface (Ti) became darker with time due to the plating of PANI (Figure S15, Supporting Information). In terms of stability, it can be seen that the current density reached its peak at 13.6 mA cm^{-2} at 0.6 h and then dropped to 12 mA cm^{-2} after 2.3 h (Figure 3c). This is likely to be due to the degradation of perovskite solar cell-based photoanode, as confirmed by the second J–V measurement after 2.3 h (see dashed curve in Figure S14, Supporting Information). The power utilization ratio was initially 83.1% and increased to 94.6% toward the end of the process even after the degradation of the perovskite solar cell photoanode. This suggests that the initial power supplied by the fresh cell was more than what the process required. The lower bias required for this new process is significant as it is one of the very first to require only one solar cell for H_2 generation while other state-the-art solar-driven-H_2 production processes require the use of multiple single junction solar cell in series or the use of multi-junction tandems (Table S3, Supporting Information).

To demonstrate the feasibility of using earth abundant HER catalyst replacing Pt sheet, CoP was fabricated by electrodeposition on Ni foam[49,50] that showed good electrocatalytic ability for HER (Figure S16, Supporting Information). The morphology and composition of CoP were confirmed by SEM and energy dispersive X-ray spectroscopy (EDS) (Figure S17, Supporting Information). CoP-Ni-foam performed better than Ni-foam alone as a counter electrode (Figure S18, Supporting Information). While there is still room for improvement to match the performance of Pt electrode, CoP shows very good stability (Figure S19, Supporting Information) and therefore is a low-cost catalyst alternative for solar-driven H_2 production and ANI polymerization.

PANI is a conductive polymer with a broad molecular weight distribution. There can be three types of linkages between ANI monomer units during the polymerization process including "head-to-head", "tail-to-tail", and "head-to-tail" configurations.[30] In the last two cases, chain assembly may occur via substitution in phenyl ring with the formation of ortho-, para-, and meta- monomer units. Thus, oxidative polymerization yields chains with a wide variety of monomer unit structures. In addition, the formation of PANI polymer chain may proceed via recombination of cation radical oxidation sites or electrophilic substitution.[30] For the former, polymer growth is via polycondensation, when fragments of any length recombine. In the case of electrophilic substitution, oxidized nitrogen-containing structure substitutes one proton of the phenyl ring of another aniline molecule. All of these pose challenge to determine the Gibbs free energy or the theoretical minimum potential for the ANI polymerization initiation reaction. For a rudimentary determination of solar-to-hydrogen conversion efficiency (η_{STH}), 1.05 V [30–32,37] was assumed for initiating ANI

polymerization reaction. This gives a theoretical maximum (see calculation method in the Experimental Section) of 15.5% for the process driven by the external 2-half-cell-in-series silicon PV device or 14.4% for the process driven by the integrated perovskite-solar cell-based photoanode. These values are likely to be overestimated as the theoretical bias (to be determined in future work) required for polymerization initiation will likely to be lower than 1.05 V. If a 27% loss was assumed in the system, i.e., assuming 0.76 V required for the polymerization initiation, then the η_{STH}'s would be revised down to 11.2% and 10.4%. These η_{STH} values are listed in Table S3 (Supporting Information) and compared with some of the solar driven water splitting processes reported. The use of a single perovskite cell in our process is advantageous without having to dissect a cell into multiple sections that then need to be reconnected in series for other processes reported requiring high voltage bias.[51,52] The self-regulatory nature of our process together with the eliminations of acid replacement step and ion-selective membrane represent significant cost savings compared to the traditional approach for solar-driven-H_2 production with an added advantage of co-production of value-add product.

3. Conclusion

In summary, we have developed a solar-driven co-production of H_2 and value-add conductive polymer PANI that is 10 to 1000 times more valuable than the O_2 that is normally generated in conventional water splitting. The lower operational bias means one single junction perovskite solar cell can be used for H_2 production while inhibiting any oxygen evolution reaction at the anode. The product PANI is solid that is easily harvestable and can be electroplated onto surface of interest. Therefore, the process does not require the use of a separation membrane. The polymerization being a proton releasing process eliminates the need for acid replenishment. In addition, the process is auto-catalytic and self-regulates when driven by solar. All these benefits reduce both the cost and complexity of the process significantly. The ANI polymerization process has a high-power utilization ratio of 93%, while the Faradaic efficiency for H_2 production is 98.6 ± 3.9%. Last, the use of low-cost earth-abundant CoP-Ni foam replacing Pt as counter electrode for the process was demonstrated. This work is an advancement for low-cost solar-driven production of H_2 incorporating simultaneous high value product co-generation in one process accelerating development for rapid transformation to clean H_2 economy.

4. Experimental Section

Si Photovoltaic Device: A 6 inch Monocrystalline 4 busbar (BB) monocrystalline silicon solar cell with 180 µm thickness (Shenzhen Xiangxinrui Solar Energy Co., Ltd) was cut into small stripes of 1 cm × 2 cm by FOBA M1000 laser. The SnPb-coated copper tab wires of 1 mm × 0.2 mm (Jiangsu Clelo Material Technolgoies Co. Limit) were used to connect two stripes in series forming an encapsulated PV device. External feedthroughs for the front and rear metallizations were soldered with a chisel tip (Ryobi Australia) after 951 soldering flux was applied using a Kester flux pen. The PV device was encapsulated between two glass slides using black tapes. Apertures were in the form of two times 0.4 cm^2 for illumination to drive the ANI polymerization process.

Fabrication of Perovskite Solar Cell: The perovskite solar cell with a p–i–n structure consisted of Glass/NiO$_x$/PTAA/perovskite/C60/BCP/Ag was fabricated. NiO/PTAA (PTAA = Poly[bis(4-phenyl)(2,4,6-trimethylphenyl) amine], poly(triaryl amine) stack acted as the hole transporter layer, C60 acted as the electron layers while BCP (BCP = Bathocuproine) acted as the buffer layer.

To complete the perovskite solar cell fabrication, the patterned ITO-coated glass was first cleaned by sonication in de-ionized water with 2% Hellmanex, de-ionized water, acetone, and isopropanol. NiO$_x$(10 nm) was then deposited in an AJA International sputtering system with a 30 W of RF power and pure Ar at 2.0 mTorr. Samples were then transferred to N$_2$ filled glovebox for subsequent depositions. A PTAA (Sigma) solution (2 mg mL^{-1} in chlorobenzene ((Alfa Aesar))) was first spin-coated on the NiO layer at 4000 rpm for 30 s followed by annealling at 100 °C for 10 min.

To prepare perovskite precursor solution, FAI (1 M, GreatCell Solar), PbI$_2$ (1.1 M, TCI), MABr (0.2 M, GreatCell Solar), and PbBr$_2$ (0.2 M, TCI) were dissolved in a mixed solvent of *N, N*-dimethylformamide (Alfa Aesar) and dimethyl sulfoxide (Alfa Aesar) (4:1 v/v). The precursor was spin-coated on PTAA layer at 2000 rpm for 20 s, followed by 6000 rpm for 30 s. During the spin-coating, chlorobenzene was quickly dispensed 5 s before the end of the spin process. The film was annealed at 100 °C for 10 min producing a dark brown dense perovskite film. Twenty five nanometers of C60 (Lumtec >99.5%) and 6 nm of BCP (Lumtec) layers were then thermally deposited without breaking the vacuum. Finally, 100 nm of Ag metal electrode was deposited by thermal evaporation through a metal mask to complete the perovskite solar cell fabrication.

Integrating Perovskite Solar Cell as a Photoanode: Details of encapsulating the perovskite solar cell using polyisobutylene (PIB) can be found in the previously published paper.[49] On the exposed hole transporting ITO side of perovskite solar cell, Ag paste was applied for attaching a piece of Ti foil (≈1 cm^2) as an ohmic contact for ANI polymerization. The other exposed electron transporting Ag side of the perovskite solar cells was ohmically connected with a wire using Ag paste. Finally, all the exposed conductive area was coated with araldite glue to avoid direct contact with the electrolyte. The irradiated area was quantified by the imageJ software.

Electrochemical Reaction: The set up for the ANI polymerization process consists of a custom-made gas-tight one-compartment photoelectrochemical reactor (pre-flushed using ultra-high purity He gas for ≈1 h to remove contaminant) with a quartz window in a two-electrode configuration connected to an eDAQ-ERR 466 potentiostat, illuminated by 100 W Xenon lamp (Solar Light, XPS-400) with an AM 1.5G filter at 1 sun irradiation. The working electrode, being the anode, consisted of a piece of FTO-glass or Ti sheet or perovskite solar cell-based photoanode. The counter electrode, being the cathode, consisted of a Pt sheet or CoP-Ni foam. The electrolyte was an aqueous 0.1 or 0.5 M H$_2$SO$_4$ solution in which was dissolved 0.1 or 0.2 M of aniline (ANI). The potentiostat was used to record the passing current during the ANI polymerization process when the PV device drove the reaction. The applied potential was 0 V versus the counter electrode for two-electrode configuration with a potentiostat recording the passing current.

Quantifying H$_2$ Evolution: H$_2$ evolution was quantified by a gas chromatograph (GC, Shimadzu 2030, 5 Å molecular sieve column) equipped with a discharge ionizatioin detector (Vici pulsed discharge ionization detector D D-4-I-SH14-R; detection limit in the low ppb range) using a constant 30 mL min^{-1} of He as the carrying gas through the reactor. First, five different concentrations of H$_2$ gas were first injected into the GC instrument to measure their corresponding H$_2$ peak areas. Then, a linear calibration curve was established based on the already known H$_2$ concentration and their corresponding H$_2$ GC peak area. In a typical measurement of Faradaic efficiency, the amount of H$_2$ gas evolved from the reactor was measured by the GC every 10 min. The concentration of H$_2$ production rate can be deduced through fitting the H$_2$ GC peak area onto the H$_2$ calibration curve. At the same time, the passing charges for each GC retention time (10 min in the experiment) can be obtained through a potentiostat. Assuming all the passing charges were used for H$_2$ evolution, the amount of H$_2$ gas could be calculated.

Determining Proton Releasing Sources: For this experiment, N$_2$ and H$_2$ controls, and sampled gasses from (i) deuterium labeled ANI polymerization reaction (ANI in atom D deuterium oxide (D$_2$O)) and sulfuric acid-D$_2$ solution (D$_2$SO$_4$)) and (ii) ANI polymerization reaction (in H$_2$O+H$_2$SO$_4$) were analyzed using GC-MS. The sample gases were taken from the reactor and injected into the sealed N$_2$-filled glass vials using a syringe for the GC-MS analysis. GC-MS spectra were collected by PerkinElmer Clarus 680 (GC) and PerkinElmer Clarus SQ 8 C (MS). The operational parameters are: Sample injection: 1 mL headspace; Injection port temperature at 250 °C; Injection sampling: 10: 1 split; Carrier gas: Helium at 3 mL min^{-1}; GC Oven program: 40 °C Isotermal for 8 min run; GC Column: Supelco Carboxen 1010 Plot column 30 m x 0.53 mm internal diameter (x250 µm film thickness); GC/MS interface temperature: 250 °C; MS Source: Positive ion EI (70 eV); MS source temperature: 150 °C; and MS scan settings: Selected ion reaction monitoring of 5, 6, 29, 30 *m/z* with 50 ms dwell time and 100 ms interchannel delay.

Calculating Faradaic Efficiency: Faradaic efficiency = Amount of H$_2$ deduced from GC peak area/ Amount of H$_2$ calculated by the passing charge × 100%.

Electrodeposition of CoP Catalysts on Ni Foam: A three-electrode configuration was used for the deposition of CoP on Ni foam, in which an Ag/AgCl (3 M KCl) electrode was used as the reference electrode, Pt sheet as counter electrode, and the Ni foam as working electrode. The Ni foam was first immersed in the N$_2$-saturated electrolyte solution containing 50 mM CoSO$_4$, 0.5 M NaH$_2$PO$_2$, and 0.1 M NaAc, and then applied a constant potential of −1.1 V versus Ag/AgCl for 20 min.

Calculating Solar-to-Hydrogen Efficiency: The solar-to-hydrogen efficiency was calculated based on the equation: STH = [J$_{sc}$ (mA cm^{-2}) × 1.05 V × η_F]/P(mW cm^{-2}), where J$_{sc}$ is the short-circuit photocurrent density, η_F is the Faradaic efficiency, P is the total integrated power input density under AM 1.5G.

PANI Characterizations: The morphology and EDS were investigated using FIB-SSEM (FESEM) at 3 kV.

Raman spectrum was measured with a Renishaw InVia Qontor Dual Raman System with Inverted and Upright Microscopes using 633 nm laser as the excitation line.

FTIR spectrum was obtained using a Bruker LUMOS FTIR.

Molecular weight distributions of the PANI were determined by size exclusion chromatography (SEC) using (DMAc) or (THF) as solvent and using the Shimadzu modular system composed of an SIL-20A auto-injector, a Polymer Laboratories 5.0 µm bead-size guard column (50 × 7.5 mm^2) followed by three linear PL (Styragel) columns (10^5, 10^4, and 10^3) and an RID-10A differential refractive-index (RI) detector for SEC-DMAc or four linear PL (Styragel) columns (10^5, 10^4, 10^3, and 500 Å), and a RI detector for SEC-THF. The eluent was either DMAc (containing 0.03% w/v LiBr and 0.05% w/v 2,6-dibutyl-4-methylphenol (BHT)) at 50 °C, run at a flow rate of 1.0 mL min^{-1} or THF at 40 °C, run at a flow rate of 1.0 mL min^{-1}. The SEC was calibrated using narrow polystyrene standards with molecular weights of 200 to 1 × 10^6 g mol^{-1}.

Solid-state NMR spectrum was recorded using a 300 MHz Bruker Avance III NMR system on a wide bore magnet for solid-state NMR.

XPS spectra were measured at 1.0 × 10^{-8} mbar by Thermo Scientific K-Alpha X-ray Photoelectron Spectrometer (XPS) System. A calibrated (C 1s = 284.8 eV) compensating electron flood gun was used to neutralize a surface charge. The high-resolution (0.1 eV resolution) spectra were obtained by 80 um X-ray beam spot at constant pass energy of 50 eV.

Calculating Polymerization Yield: The PANI product was first collected by physical scratching of the electrode followed by centrifuging (Nalgene thick wall 50 mL tube, 3000 rpm) of the precipitate in the reactor. After that, PANI product was neutralized with dilute ammonia solution (<0.1% w/v). After sonication for 20 min, PANI precipitate was recollected through centrifuging (Thermo Scientific Heraeus Biofuge Stratos, 12 000 rpm) and washing several times by DI water. Finally, the PANI precipitate was dried in an oven at 80 °C overnight. Polymerization yield was calculated by: PANI yield = mass of PANI / mass of ANI precursor × 100%.

Supporting Information

Supporting Information is available from the Wiley Online Library or from the author.

Acknowledgements

Conflict of Interest

The authors declare no conflict of interest.

Data Availability Statement

The data that support the findings of this study are available from the corresponding author upon reasonable request.

Keywords

[1] J. H. Kim, D. Hansora, P. Sharma, J.-W. Jang, J. S. Lee, *Chem. Soc. Rev.* **2019**, *48*, 1908.

[2] M. G. Walter, E. L. Warren, J. R. McKone, S. W. Boettcher, Q. Mi, E. A. Santori, N. S. Lewis, *Chem. Rev.* **2010**, *110*, 6446.

[3] W. J. Chang, K.-H. Lee, H. Ha, K. Jin, G. Kim, S.-T. Hwang, H.-m. Lee, S.-W. Ahn, W. Yoon, H. Seo, J. S. Hong, Y. K. Go, J.-I. Ha, K. T. Nam, D. Principle, L. E. f. P.–E. C. System, *ACS Omega* **2017**, *2*, 1009.

[4] D. Xu, M. B. Stevens, M. R. Cosby, S. Z. Oener, A. M. Smith, L. J. Enman, K. E. Ayers, C. B. Capuano, J. N. Renner, N. Danilovic, Y. Li, H. Wang, Q. Zhang, S. W. Boettcher, *ACS Catal.* **2019**, *9*, 7.

[5] M. A. Green, A. W. Y. Ho-Baillie, *ACS Energy Lett.* **2019**, *4*, 1639.

[6] K. Sayama, *ACS Energy Lett.* **2018**, *3*, 1093.

[7] S. Jin, *ACS Energy Lett.* **2018**, *3*, 2610.

[8] X. Shi, Y. Zhang, S. Siahrostami, X. Zheng, *Adv. Energy Mater.* **2018**, *8*, 1801158.

[9] K. Zhang, J. Liu, L. Wang, B. Jin, X. Yang, S. Zhang, J. H. Park, *J. Am. Chem. Soc.* **2020**, *142*, 8641.

[10] K. Fuku, Y. Miyase, Y. Miseki, T. Funaki, T. Gunji, K. Sayama, *Chem. Asian J.* **2017**, *12*, 1111.

[11] K. Fuku, Y. Miyase, Y. Miseki, T. Gunji, K. Sayama, WO$_3$/BiVO$_4$ photoanode coated with mesoporous Al$_2$O$_3$ layer for oxidative production of hydrogen peroxide from water with high selectivity, *RSC Adv.* **2017**, *7*, 47619.

[12] K. Fuku, K. Sayama, *Chem. Commun.* **2016**, *52*, 5406.

[13] Q. Mi, A. Zhanaidarova, B. S. Brunschwig, H. B. Gray, N. S. Lewis, *Energy Environ. Sci.* **2012**, *5*, 5694.

[14] J. Desilvestro, M. Grätzel, *J. Electroanal. Chem. Interf. Electrochem.* **1987**, *238*, 129.

[15] T. Nakajima, A. Hagino, T. Nakamura, T. Tsuchiya, K. Sayama, *J. Mater. Chem. A* **2016**, *4*, 17809.

[16] K. Fuku, N. Wang, Y. Miseki, T. Funaki, K. Sayama, *ChemSusChem* **2015**, *8*, 1593.

[17] S. Okunaka, Y. Miseki, K. Sayama, *Catal. Sci. Technol.* **2021**, *11*, 5467.

[18] S. Iguchi, H. Tateno, S. Takasugi, Y. Miseki, K. Sayama, *Sustain. Energy Fuels* **2019**, *3*, 3441.

[19] W. Luo, Z. Yang, Z. Li, J. Zhang, J. Liu, Z. Zhao, Z. Wang, S. Yan, T. Yu, Z. Zou, *Energy Environ. Sci.* **2011**, *4*, 4046.

[20] S. Iguchi, Y. Miseki, K. Sayama, *Sustain. Energy Fuels* **2018**, *2*, 155.

[21] T. Nakajima, M. Kanaori, A. Hagino, H. Tateno, T. Tsuchiya, K. Sayama, *J. Mater. Chem. A* **2018**, *6*, 110.

[22] T. Nakajima, M. Kanaori, H. Tateno, J. Nomoto, Y. Miseki, T. Tsuchiya, K. Sayama, *Sustain. Energy Fuels* **2019**, *3*, 2380.

[23] H. G. Cha, K.-S. Choi, *Nat. Chem.* **2015**, *7*, 328.

[24] X. Shi, S. Siahrostami, G.-L. Li, Y. Zhang, P. Chakthranont, F. Studt, T. F. Jaramillo, X. Zheng, J. K. Nørskov, *Nat. Comm.* **2017**, *8*, 701.

[25] T. H. Jeon, H. Kim, H.-i. Kim, W. Choi, *Energy Environ. Sci.* **2020**, *13*, 1730.

[26] T. H. Jeon, B. Kim, C. Kim, C. Xia, H. Wang, P. J. J. Alvarez, W. Choi, *Energy Environ. Sci.* **2021**, *14*, 3110.

[27] J. Stejskal, M. Trchová, P. Bober, P. Humpolíček, V. Kašpárková, I. Sapurina, M. A. Shishov, M. Varga, *Conducting Polymers: Polyaniline, Encyclopedia of Polymer Science and Technology*, pp. 1–44.

[28] G. Ćirić-Marjanović, *Polyaniline Nanostructures, Nanostructured Conductive Polymers*, pp. 19–98.

[29] C. O. Baker, X. Huang, W. Nelson, R. B. Kaner, *Chem. Soc. Rev.* **2017**, *46*, 1510.

[30] I. Sapurina, M. A. Shishov, *Oxidative Polymerization of Aniline: Molecular Synthesis of Polyaniline and the Formation of Supramolecular Structures*, IntechOpen, London, UK 2012.

[31] X.-G. Li, M.-R. Huang, W. Duan, Y.-L. Yang, *Chem. Rev.* **2002**, *102*, 2925.

[32] K. Ramalingam, S. Panchu, A. S. Salunke, K. Muthukumar, A. Ramanujam, S. Muthiah, *ChemistrySelect* **2016**, *1*, 4814.

[33] S. Lu, B. Zhao, M. Chen, L. Wang, X.-Z. Fu, J.-L. Luo, *Int. J. Hydrog. Energy* **2020**, *45*, 22419.

[34] Z. D. Zujovic, G. A. Bowmaker, H. D. Tran, R. B. Kaner, *Synth. Met.* **2009**, *159*, 710.

[35] S. Kaplan, E. M. Conwell, A. F. Richter, A. G. MacDiarmid, *J. Am. Chem. Soc.* **1988**, *110*, 7647.

[36] Z. D. Zujovic, M. R. Gizdavic-Nikolaidis, P. A. Kilmartin, H. Idriss, S. D. Senanayake, G. A. Bowmaker, *Polymer* **2006**, *47*, 1166.

[37] L. Y. O. Yang, C. Chang, S. Liu, C. Wu, S. L. Yau, *J. Am. Chem. Soc.* **2007**, *129*, 8076.

[38] D. E. Stilwell, S. M. Park, *J. Electrochem. Soc.* **1988**, *135*, 2254.

[39] T. Kobayashi, H. Yoneyama, H. Tamura, *J. Electroanal. Chem.* **1984**, *177*, 293.

[40] G. Horányi, G. Inzelt, *J. Electroanal. Chem.* **1989**, *264*, 259.

[41] A. M. P. Hussain, A. Kumar, *Bull. Mater. Sci* **2003**, *26*, 329.

[42] A. Korent, K. Žagar Soderžnik, S. Šturm, K. Žužek Rožman, *J. Electrochem. Soc.* **2020**, *167*, 106504.

[43] I. Sapurina, J. Stejskal, *Polym. Int.* **2008**, *57*, 1295.

[44] C. C. L. McCrory, S. Jung, J. C. Peters, T. F. Jaramillo, *J. Am. Chem. Soc.* **2013**, *135*, 16977.

[45] I. Roger, M. A. Shipman, M. D. Symes, *Nat. Rev. Chem.* **2017**, *1*, 0003.

[46] N.-T. Suen, S.-F. Hung, Q. Quan, N. Zhang, Y.-J. Xu, H. M. Chen, *Chem. Soc. Rev.* **2017**, *46*, 337.

[47] L. An, C. Wei, M. Lu, H. Liu, Y. Chen, G. G. Scherer, A. C. Fisher, P. Xi, Z. J. Xu, C.-H. Yan, *Adv. Mater.* **2021**, *33*, 2006328.

[48] Z. Lei, T. Wang, B. Zhao, W. Cai, Y. Liu, S. Jiao, Q. Li, R. Cao, M. Liu, *Adv. Energy Mater.* **2020**, *10*, 2000478.

[49] H. Chen, M. Zhang, T. Tran-Phu, R. Bo, L. Shi, I. Di Bernardo, J. Bing, J. Pan, S. Singh, J. Lipton-Duffin, T. Wu, R. Amal, S. Huang, A. W. Y. Ho-Baillie, A. Tricoli, *Adv. Funct. Mater.* **2021**, *31*, 2008245.

[50] H. Chen, T. Tran-Phu, P. Phang, R. Bo, D. Yan, D. MacDonald, A. Tricoli, *Adv. Energy Sustainability Res.* **2021**, *2*, 2100012.

[51] S. Y. Reece, J. A. Hamel, K. Sung, T. D. Jarvi, A. J. Esswein, J. J. H. Pijpers, D. G. Nocera, *Science* **2011**, *334*, 645.

[52] C. R. Cox, J. Z. Lee, D. G. Nocera, T. Buonassisi, *Proc. Natl. Acad. Sci. USA* **2014**, *111*, 14057.